

Geo-Congress 2026

GSP 375

Earthquake Engineering and Soil Dynamics

Selected Papers from Geo-Congress 2026
Salt Lake City, Utah | March 9–12, 2026

Edited by
Jack Montgomery, Ph.D., P.E.
Brady R. Cox, Ph.D., P.E.

ASCE
G-I GEO-INSTITUTE ASCE

GEOTECHNICAL SPECIAL PUBLICATION NO. 375

GEO-CONGRESS 2026

EARTHQUAKE ENGINEERING AND SOIL DYNAMICS

SELECTED PAPERS FROM SESSIONS OF GEO-CONGRESS 2026

March 9–12, 2026
Salt Lake City, Utah

SPONSORED BY

The Geo-Institute
of the American Society of Civil Engineers

EDITED BY
Jack Montgomery, Ph.D., P.E.
Brady R. Cox, Ph.D., P.E.

Published by the American Society of Civil Engineers

Published by American Society of Civil Engineers
1801 Alexander Bell Drive
Reston, Virginia, 20191-4382
www.asce.org/publications | ascelibrary.org

Any statements expressed in these materials are those of the individual authors and do not necessarily represent the views of ASCE, which takes no responsibility for any statement made herein. No reference made in this publication to any specific method, product, process, or service constitutes or implies an endorsement, recommendation, or warranty thereof by ASCE. The materials are for general information only and do not represent a standard of ASCE, nor are they intended as a reference in purchase specifications, contracts, regulations, statutes, or any other legal document. ASCE makes no representation or warranty of any kind, whether express or implied, concerning the accuracy, completeness, suitability, or utility of any information, apparatus, product, or process discussed in this publication, and assumes no liability therefor. The information contained in these materials should not be used without first securing competent advice with respect to its suitability for any general or specific application. Anyone utilizing such information assumes all liability arising from such use, including but not limited to infringement of any patent or patents.

ASCE and American Society of Civil Engineers—Registered in U.S. Patent and Trademark Office.

Photocopies and permissions. Permission to photocopy or reproduce material from ASCE publications can be requested by sending an e-mail to permissions@asce.org or by locating a title in ASCE's Civil Engineering Database (http://cedb.asce.org) or ASCE Library (http://ascelibrary.org) and using the "Permissions" link.

Errata: **Errata, if any, can be found at https://doi.org/10.1061/9780784486702**

Copyright © 2026 by the American Society of Civil Engineers.
All Rights Reserved.
ISBN 978-0-7844-8670-2 (PDF)
Manufactured in the United States of America.

Preface

This is the first volume of seven Geotechnical Special Publications (GSPs) containing papers from Geo-Congress 2026: Geo Tools, Technologies, and Techniques in an Environment of Change, held in Salt Lake City, Utah, on March 9-12, 2026. Notably, this conference marks the 30th anniversary of the Geo-Institute. The conference brought together industry leaders, researchers, and practitioners to showcase innovations, address critical challenges, and advance knowledge in geotechnical engineering. The conference hosted the Terzaghi, Peck, Seed, and Prakash Lectures and many technical sessions, panel sessions, short courses, and student competitions.

These proceedings represent the culmination of nearly two years of effort by the program committee and many other individuals, whose focus has been to continue the success of previous Geo-Congresses and to celebrate 30 years of geotechnical innovation by the Geo-Institute. Building the program started with an international call for papers that resulted in more than 800 abstracts on a variety of important topics. Each paper was subjected to a rigorous technical review by two or more independent peer reviewers. Acceptance required concurrence by at least two peer reviewers, and final decisions were made only after review coordinators confirmed that authors satisfactorily addressed any reviewer comments on their original submission. All accepted papers are presented at the conference as posters or technical talks and are eligible for applicable ASCE awards.

This volume contains a collection of 57 papers focused primarily on the topics of earthquake engineering and soil dynamics. This includes papers on seismic liquefaction, site response, soil-structure interaction, and risk assessment.

The success of this conference and proceedings would not have been possible without the participation and collaboration of many individuals, including Brad Keelor, the tireless staff at the Geo-Institute, and the many session chairs and reviewers. We hope that these proceedings will be of use to the geotechnical engineering community for many years to come.

The Editors,

Jack Montgomery, Ph.D., P.E., M.ASCE, Auburn University
Brady R. Cox, Ph.D., P.E., M.ASCE, Utah State University

© ASCE

Acknowledgments

We are very grateful for the contributions of the authors, peer reviewers, session chairs, and program committee, without whom this publication would not be possible.

Geo-Congress 2026 Conference Program Committee

Conference Chairs
K. N. Gunalan, Ph.D., P.E., BC.GE, Pres. 20 ASCE, NAC, HNTB Corporation
Ryan B. Maw, P.E., G.E., BC.GE, F.ASCE, Gerhart Cole

Technical Chair
Shideh Dashti, Ph.D., M.ASCE, University of Colorado Boulder

Proceedings Editors
Brady R. Cox, Ph.D., P.E., M.ASCE, Utah State University
Jack Montgomery, Ph.D., P.E., M.ASCE, Auburn University

Student Program Liaison
Cassandra Rutherford, Ph.D., P.E., M.ASCE, Iowa State University

Program Committee Members
Aaron L. Leopold, P.E., M.ASCE, Dan Brown and Associates
Kam Ng, Ph.D., P.E., M.ASCE, University of Wyoming
Jenny Ramirez, Ph.D., P.E., M.ASCE, Geosyntec Consultants

© ASCE

Contents

A Database of Aftershock Ground Motions Recorded by the I-15 Downhole Array Following the 2020 M5.7 Magna, Utah, Earthquake 1
Tyler S. Jackson and Brady R. Cox

A Dataset of Microtremor Horizontal-to-Vertical Spectral Ratio (mHVSR) Measurements Collected at Strong Motion Stations that Recorded the 2020 M5.7 Magna, Utah, Earthquake 11
Kyle S. Cannon and Brady R. Cox

A Machine Learning Framework for Predicting Liquefaction Ejecta Severity 21
Lianne Brito, Shideh Dashti, Abbie B. Liel, and Brad P. Wham

Addressing the Needs and Challenges in Evaluating Liquefaction: A Survey of the State of Practice 32
Kristin J. Ulmer, Scott J. Brandenberg, Kenneth S. Hudson, Paolo Zimmaro, Steven L. Kramer, and Jonathan P. Stewart

Application of Machine Learning for Identification of Hidden Rock Sites Using Earthquake Records 41
Michael R. Dupuis

Assessment of Restricted Zone for Blast Induced Liquefaction and Its Effect on Nearby Slopes 51
Karan Gupta, Tapobrata Lodh, and Kaustav Chatterjee

Automated Workflow for 3D Site Response Analysis with Complex Stratigraphy Using LS-DYNA 62
Yizhen Yan, Ian Bruce, Kirk Ellison, Pawan Kumar, and Rica Chen

Calibration of Pressure-Dependent Multi-Yield Surface Constitutive Soil Model for Undrained Cyclic Shear Behavior of Low Plasticity Silt 73
Arash Khosravifar and Benyamin Jalilnavaznovin

Case Study: Liquefaction Evaluation and Comparison with Reconnaissance Observations in the Port of Manta after the Mw 7.8 Earthquake of April 16, 2016, in Pedernales, Muisne, Ecuador 83
Karina E. Roman and Santiago R. Caballero

Comparative Analysis of Seismic Hazard Parameters in India: A Dual-Scale Approach 95
Arindam Das, Ranjit Das, and Deepankar Choudhury

© ASCE

Comparing Liquefaction Hazard Assessment Methods for Fuel Storage Facilities in Portland's CEI Hub 106
Ana C. Tijerina Esquino, Diane Moug, Arash Khosravifar, and David Yang

CPT-Based Probabilistic Assessment of Seismic Soil Liquefaction Triggering Relationships 116
Gizem Can, Kemal O. Cetin, Robb E. S. Moss, Robert E. Kayen, Makbule Ilgac, and B. Umut Ayhan

Design and Integration of a Pneumatic Rainfall System with Seismic Shaking in a Geotechnical Centrifuge 127
Amir Alam Sayari, Ian McLeod, and Shideh Dashti

Dynamic Response of Sheet-Pile Wall with Liquefiable Backfill 138
Aya Abuo Zenab, Vishwas A. Sawant, Akanksha Tyagi, and Ali Mayya

Effect of Axle Configuration on Railway-Induced Vibrations 149
Tapan Suyal and B. K. Maheshwari

Effect of Overburden Stress on Cyclic Resistance of Fine-Grained Materials 160
Varun N. S. Renugah, Arda Sahin, Amalesh Jana, Kristin J. Ulmer, Scott J. Brandenberg, Jonathan P. Stewart, Armin W. Stuedlein, T. Matthew Evans, and Steven L. Kramer

Effect of Pre-Shaking on Shear Modulus Degradation during Four Strong Shaking Events Using Shaking Table Tests 171
Roohollah Farzalizadeh, Abdolreza Osouli, and Prabir Kolay

Effects of Near-Fault Ground Motions on Liquefaction-Induced Building Settlement at the Port of Wellington, New Zealand 181
William Z. Zakka and Jonathan D. Bray

Evaluating the Impacts of Soil Layering on the Dynamic Response of a Structure 191
Alireza Kazem and Lisa M. Star

Evaluation of New and Existing Shear Modulus Reduction Models to Predict Measured In Situ G/G_{max} in Transitional Silts 202
Besrat E. Alemu, Armin W. Stuedlein, Zhongze Xu, and Kenneth H. Stokoe II

Examination of Undrained Cyclic Shear Behavior of Montanan Varved Lacustrine Fines 213
Bret Lingwall, Tyler Quick, Tyler Chatfield, and James Olsen

HVSR-Based Seismic Site Classification Using K-Means Clustering 223
Sanidhya Sharma and Weiwei Zhan

© ASCE

Influence of Superstructure Height on the Seismic Response of Pile-Supported Structures with Consideration of Soil–Pile–Structure Interaction 233
Arezoo Sadrinezhad and Matthew Mendoza

Input Motion Selection for Large-Scale Shake Table Tests to Evaluate Kinematic Soil–Structure Interaction Effects 243
Reza Mohammadi, Kevin Stanton, and Ramin Motamed

Liquefaction and Flowability Properties of Sand with Strain History 253
Prakash Badu, Gurusamy Kalaiselvan, Amalesh Jana, and Mohammad Khosravi

Machine Learning-Assisted Calibration of Plasticity Models for Liquefiable Geosystems 264
Maziar Mivehchi, Laura Luna, and Katerina Ziotopoulou

Mitigating Vibration Impact of Proposed Kathmandu Valley Metro through Numerical Modeling 274
A. Tiwari, S. Acharya, and R. C. Tiwari

Mitigation of Soil Reliquefaction Using Prefabricated Vertical Drains under Repeated Seismic Shaking 284
Gowtham Padmanabhan, B. K. Maheshwari, and Tapan Suyal

Modeling of Strain-Rate Effects and Its Implications on the Lateral Spreading of Liquefiable Soils 294
Mohamed A. ElGhoraiby and Majid T. Manzari

Next Generation Probabilistic Liquefaction Model Building at the Regional Scale 305
Jonathan Schmidt, Shideh Dashti, and Cristina Torres-Machi

NGL Liquefaction Triggering Model—Virginia Tech Modeling Team: Updates to Defining σ_ε and Resolving Sampling Bias 314
Tat Shing Thum, Adrian Rodriguez-Marek, Russell A. Green, and Peter J. Stafford

Numerical Investigation of the Effect of Using Geofoam on Static and Dynamic Earth Pressures Affecting Retaining Structures 325
Yusuf Kayan, Abdirahman Y. Duale, and Selçuk Bildik

Observations and Interpretation from a Centrifuge Test on a Pile-Supported Wharf Subjected to Combined Superstructure Inertia and Lateral Ground Deformations 336
Andrew Earl Parrott, Arash Khosravifar, Benyamin Jalilnavaznovin, Stephen Dickenson, Nason McCullough, and Scott Schlechter

© ASCE

Probabilistic Framework for Seismic Fragility Analysis of Nuclear Power Plants under Earthquake Hazards **347**
Lei Wang and Skarleth Gutierrez

Proxy-Based V_{S30} Estimation for Utah Conditioned on Surface Geology and Surface Gradient **355**
Joseph Choi, Jonathan P. Stewart, Tristan E. Buckreis, and Scott J. Brandenberg

Quantitative Soil Behavior Type Assessment from Cyclic Test Results **365**
Arda Sahin, Amalesh Jana, Kristin J. Ulmer, Scott J. Brandenberg, T. Matthew Evans, Armin W. Stuedlein, Steven L. Kramer, and Jonathan P. Stewart

Repeatable Source, Site, and Path Effects on Ground Motion Median and Variability Based on Dataset from the Central and Eastern United States **376**
Mehran Davatgari-Tafreshi and Shahram Pezeshk

Seismic Displacement Hazard and Earth Dam on a Soft Foundation **386**
Franklin Olaya and Luis Cañabi

Seismic Response of Soft Soil Reinforced with SC Grids: Centrifuge Experiments and Numerical Investigations **396**
S. Devkota, M. Khosravi, K. Mohammadi, and A. Khosravi

Shake Table Studies of a Geotechnical Seismic Isolation System Using Lightweight Expanded Clay Aggregates **406**
Farmehr M. Dehkordi, Farzad Naseri, and Fariborz M. Tehrani

Site and Basin Effects in the Central and Eastern US: City- and State-Scale Evaluations in Memphis, New York City, and Massachusetts **416**
James Kaklamanos, Laurie G. Baise, Christina Sanon, Elise H. Meyer, Irvin M. Guzman, and George A. Sachs-Walor

Site Characterization for Selected Liquefaction Case History Sites from February 6, 2023, Türkiye-Kahramanmaras Earthquakes **427**
Arda Sahin, Robb Eric S. Moss, Kemal Onder Cetin, Scott J. Brandenberg, and Jonathan P. Stewart

Site Response for Nearly Vertical Incident P and SV Waves **439**
Santosh Katuwal and Renmin Pretell

Site-Specific Liquefaction Fragility Functions for Probabilistic Liquefaction Hazard Analysis **448**
Michael W. Greenfield and Timothy Estep

© ASCE

Small-Strain Shear Modulus and Damping Ratio Models for Southeastern US Residual Soil and Saprolite Considering Loading Frequency....457
Hossein Golkarfard and Ronald D. Andrus

The Critical Role of Initial Stresses in the Seismic Response of Sheet-Pile Walls in Liquefiable Soils....467
Sarra Lbibb and Majid T. Manzari

The Influence of Confining Stress on Liquefaction Resistance of Uniform Ottawa C109 Sand and Uniform Pea Gravel....477
Satuk Bugrahan Sari and Adda Athanasopoulos-Zekkos

The Role of Friction in Model Tests and Its Effects on the Seismic Response of Geostructures....493
Sarra Lbibb and Majid T. Manzari

Three-Dimensional Ground Response Analyses at the I-15 Downhole Array Site near Salt Lake City....504
Nishkarsha Dawadi, Tyler S. Jackson, and Brady R. Cox

Towards Improved Regional Liquefaction Hazard Assessments Using Geospatial Surrogate Models....515
Morgan D. Sanger, Mertcan Geyin, and Brett W. Maurer

Understanding Kappa (κ) for Basins of the Intermountain West: Insights from the 2020 Magna, Utah, Earthquake....524
Bret Lingwall

Effect of Spectral Matching Technique on Reinforced Concrete Pile Groups Considering Soil–Structure Interaction....534
Jatheesan Sundararajan, Ashish Bahuguna, Nadarajah Ravichandran, Ronald D. Andrus, and Nicholas E. Harmon

Updated SPT-Based Seismic Soil Liquefaction Triggering Relationships....544
Makbule Ilgac, Kemal O. Cetin, Robert E. Kayen, Robb E. S. Moss, Gizem Can, and B. Umut Ayhan

Updating CPT-Based Liquefaction Parameters through Bayesian Inference: Insights from the 1979 Imperial Valley Earthquake....554
Kannebaigari Mahammad Rafi and Pinom Ering

Validation of Tri-Directional Site Response Analysis in LS-DYNA: Case Studies of Service Hall Array in Japan....564
Alejandro Huaman, Ramin Motamed, Salman Rahimi, Kirk Ellison, and Pawan Kumar

© ASCE

Vehicle Impact Loading on Soil-Embedded Piles Installed near Slopes 579
Mojdeh Pajouh, Tewodros Yosef, Robert W. Bielenberg, and Ronald K. Faller

Validating Wharf Damage at the Port of Oakland from the 1989 Loma Prieta Earthquake: A Study of Lateral Spreading Using Earthquake Simulations.....590
Sajan K C and Chukwuebuka C. Nweke

© ASCE

A Database of Aftershock Ground Motions Recorded by the I-15 Downhole Array Following the 2020 M5.7 Magna, Utah, Earthquake

Tyler S. Jackson[1] and Brady R. Cox, Ph.D., P.E.[2]

[1]Consultant, Gerhart Cole, Inc., Midvale, UT (corresponding author).
Email: tylerj@gerhartcole.com
[2]Professor, Utah State Univ., Logan, UT. Email: brady.cox@usu.edu.

ABSTRACT

The I-15 Downhole Array (I15DA) is located near the intersection of I-15 and I-80 in Salt Lake City, Utah. It is positioned in a seismically active area near the Salt Lake City section of the Wasatch Fault and the Taylorsville section of the West Valley Fault. The downhole array is installed in soft, Lake Bonneville soil deposits where the depth to bedrock is expected to be at least 370 m. The array is made up of five, three-component force-balance accelerometers (FBA). One of the sensors was installed on the surface, and the other sensors were installed at depths of 7.6, 18.3, 48.8, and 119.8 m. Unfortunately, due to a loss of power and data buffering/telemetry issues at the site, none of these sensors fully captured the main shock of the 2020 M5.7 Magna, Utah, Earthquake, whose epicenter was located approximately 15 km north-west of the I15DA. However, the surface and deepest sensors recorded some of the aftershocks following the main event, and continuous datastreams containing approximately 61 aftershocks with magnitudes greater than 2.0 were provided to our research team by the University of Utah Seismograph Stations. The 61 aftershocks had local magnitudes (M_L) that ranged from 2.0 to 4.57, and peak ground acceleration (PGA) values for the surface sensor that ranged from less than 0.001 g to 0.132 g. Unfortunately, after processing, only eight of the aftershock events generated high enough signal-to-noise ratios (SNR) on both the surface and 120-m sensors over a bandwidth of 0.5 to 10 Hz. This paper describes the ground motion processing performed on the I15DA recordings, presents empirical transfer functions (ETFs) calculated from the ground motions, and provides a reference to an open-access database where the raw and processed ground motion records can be downloaded for use in site response studies.

INTRODUCTION

The I-15 Downhole Array (I15DA) is located near the south intersection of I-15 and I-80 in South Salt Lake City, Utah. It is located in a seismically active area of Utah and is near the Salt Lake City section of the Wasatch Fault zone and the Taylorsville section of the West Valley Fault zone. The downhole array is installed in soft lakebed soils deposited by ancient Lake Bonneville. The depth to engineering rock (Site Class B) is expected to be at least 100 meters based on deep surface wave testing at the site (Jackson 2024) and the depth to hard rock (Site Class A) is expected to be at least 370 meters based on the Community Velocity Model (CVM; Magistrale et al 2008), but possibly as deep as 875-1000 meters based on deep surface wave testing. A plan view showing the location of the I15DA and surrounding area is included in Figure 1.

The I15DA consists of five, three-component force-balance accelerometers (FBA), as follows: (a) one Kinemetrics EpiSensor FBA ES-T is installed at the surface, (b) three Kinemetrics Shallow Borehole EpiSensor (SBEPI) FBAs are installed at depths of 7.6, 18.3, and 48.8 meters, and (c) one Kinemetrics HypoSensor FBA ES-DH is installed at 119.8 meters. The FBAs are connected

© ASCE

to Kinemetrics K2 digitizers. During installation, which took place from April 2002 to April 2003 (Youd and Briggs 2003), the boreholes for the sensors were cased with PVC and grouted in place. For reference in this paper, each sensor in the I15DA has been referred to as DH (downhole) and then sequentially by increasing depth: DH_0 (surface), DH_1 (7.6 meters), DH_2 (18.3 meters), DH_3 (48.8 meters), and DH_4 (119.8 meters).

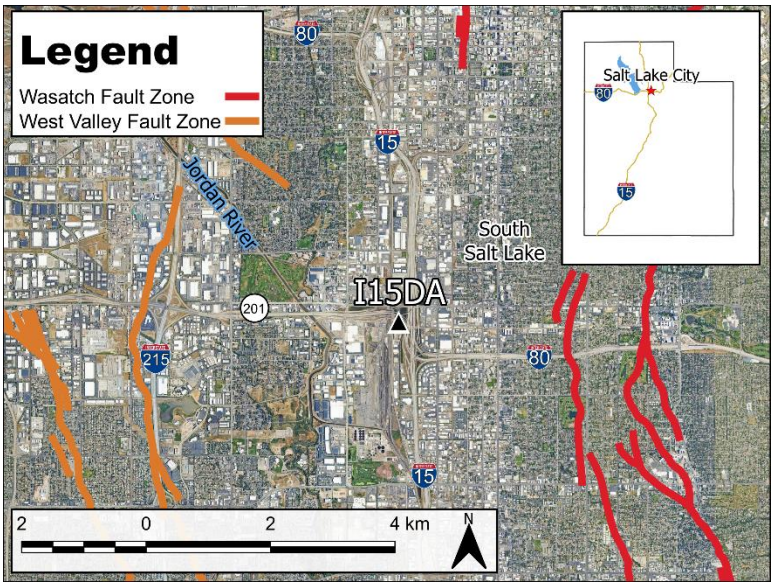


Figure 1. Plan view of the I15DA and the surrounding area in Salt Lake City, Utah. Map content sources: QGIS.org, Google, Airbus © 2025, and UGRC.

As detailed in Youd and Briggs (2003), Robert Stellar of GEOVision performed invasive PS-logging in the deepest borehole (DH_4) in two phases: from the surface to 76 meters in 2002, and from 65 to 116 meters in 2003. These measurements provide a profile of the one-dimensional shear wave velocity (Vs) structure of the I15DA site. For this research, we have elected to simplify the Vs profiles from PS-logging with a system of nine layers for use in site response calculations. Figure 2 presents the sensor depths, measured PS-logging Vs profiles, and the simplified 9-layer Vs profile alongside a lithologic log compiled from soil cuttings in the DH_4 borehole.

The sensors were set to trigger and store data when any sensor in the array sensed accelerations greater than 0.01 g. Unfortunately, due to a loss of power and data buffering/telemetry issues at the site during the main shock, none of these sensors fully captured the 2020 M5.7 Magna Earthquake. However, personnel from the University of Utah Seismograph Stations (UUSS) were able to restore functionality after several hours and initiate a continuous datastream recording for all downhole array sensors during a portion of the aftershocks following the main event. It should also be noted that SBEPI FBAs had stopped functioning properly in the years prior to the Magna Earthquake, and only stations DH_0 and DH_4 remained operational. Although not the focus of this paper, an additional nine FBAs were installed on Bridge C-846 above the I15DA site (Halling and Petty 2001). These sensors also failed to capture the main shock but recorded the same continuous datastream as the downhole array sensors following the main event.

This paper describes the ground motion processing performed on the I15DA aftershock recordings, presents the empirical transfer functions (ETFs) calculated from the ground motions recorded by sensors DH_0 and DH_4, and provides a reference to an open-access database where the

© ASCE

raw and processed ground motion records can be downloaded for use in site response studies to support efforts in better understanding and modelling seismic site response in the Salt Lake Valley.

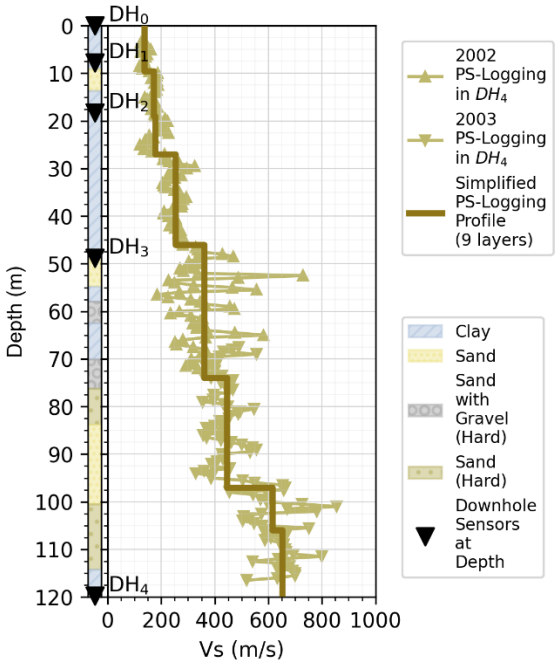


Figure 2. Lithologic soil log, invasive Vs profiles, and downhole sensor locations for the I15DA. Each downhole sensor is shown at its as-built depth to the left of the lithologic log.

GROUND MOTION PROCESSING

The continuous datastream recordings were provided to our research team through personal communication by Mr. Jon Rusho from the UUSS. The continuous data spanned from 18 March 2020 at 18:30 UTC (note that the main shock happened at approximately 13:00 UTC) to 26 March 2020 at 19:15 UTC. These continuous datastreams, as well as the processed ground motions recorded by sensors DH_0 and DH_4, are in the process of being added to an open-access database on DesignSafe (Rathje et al. 2017). Details about the ground motion processing are provided below.

Isolating Aftershock Events

The raw data was first sorted by sensor depth and component of interest. For this particular study, only the horizontal components (both North and East) recorded by the DH_0 and DH_4 sensors were considered, as the other downhole sensors were not functioning properly in the days leading up to the Magna Earthquake. Records with the prefix of "40" were recorded by the DH_4 sensor at a depth of 120 m, while records with the prefix "F0" were recorded by the DH_0 sensor on the ground surface. After this sorting, a list of aftershocks from the Magna Earthquake was obtained using the "Search Earthquake Catalog" tool provided by the ANSS Comprehensive Catalog (ComCat) on the United States Geological Survey (USGS) website. Using this list, the continuous datastreams for each component of each sensor were parsed to extract each aftershock event. The ground motion records were trimmed with a buffer of 40 seconds before and 90 seconds after each

© ASCE

ComCat catalog event start time to make sure the pre-event noise and the entire signal was captured in the event-specific traces. Using the USGS catalog of events and the raw ground motion data files, data was extracted for a total of 61 candidate aftershock events. These events had local magnitudes (M_L) that ranged from 2.0 to 4.57 and peak ground acceleration (PGA) values on sensor DH_0 that ranged from less than 0.001 to 0.132 g's.

Procedure for Ground Motion Processing

After isolating the aftershock events for each station and component of interest, each component and station for each aftershock event was processed following the procedures presented in Goulet et. al. (2021) for processing ground motions in the PEER NGA-East database. First, a visual inspection was conducted on the raw time histories to ensure the ground motion's time history was distinguishable from the sensor background noise. Time histories where the ground motion could not clearly be distinguished were omitted from further consideration. During this process, 47 of the 61 candidate ground motions were rejected, as the ground motion signal was not visually recognizable above the sensor background noise levels.

The raw ground motion time histories from the remaining 14 events then underwent the following pre-processing procedure. First, the time histories were converted to engineering units of acceleration (g's) using the digitizer and sensor response data provided by the UUSS. After visual inspection, the time history was trimmed again, if necessary, to remove errant noise around the ground motion signal. Then, a constant "de-meaning" method was used to detrend the entire time history. Next, the trace was filtered in the time domain using a 5th order Butterworth high-pass filter at a low-cut frequency of 0.01 Hz to remove undesirable low-frequency noise. The trace was then integrated twice to obtain displacement, and a 6th order polynomial baseline correction detrending was applied to the displacement time history. Finally, the time history was differentiated twice to produce the pre-processed acceleration time history.

The pre-processed acceleration time histories from the deep DH_4 sensor, also referred to as the "base" sensor, were then divided into corresponding ground motion signal windows and pre-event noise windows based on the following procedure (refer to Figure 3). First, the beginning of the base signal window, t_{Bi}, was visually determined based on the P-wave's first arrival time. The end of the base signal window, t_{Bf}, was determined by the time to 98% of the Arias Intensity, I_a, relative to the start time t_{Bi}. Thus, the signal/event duration was set equal to $t_{Bf} - t_{Bi}$. The noise window was then determined by taking the catalog event start time (which was consistently before the P-wave arrival) as the end time for the noise window, and the noise start time was determined by subtracting the length of the signal window ($t_{Bf} - t_{Bi}$) from the catalog event time. Figure 3b illustrates this procedure using the north component of USGS Event ID uu60364822, where both the signal and noise windows for the deep DH_4 sensor are shown.

In an effort to capture the complete ground motion event recorded by the base sensor on the surface sensor, the surface time history from sensor DH_0 was divided into corresponding signal windows and pre-event noise windows using the following procedure. First, for simplicity, the surface signal start time, t_{Si}, was set equal to the same time as t_{Bi}. Then, the Vs travel time between the base sensor and the surface sensor was accounted for using the simplified PS-logging Vs profile shown in Figure 2. This was done by adding the mean Vs travel time from a depth of 120 m to the surface (Δt_{SH}), which was 0.4 s, to the t_{Bf} in order to get the surface signal end time, t_{Sf}. If this Δt_{SH} adjustment was not accounted for, the entire event recorded on the base sensor would not be captured on the surface sensor. Of course, this resulted in surface windows that were 0.4 s longer

© ASCE

than base windows. This challenge was overcome through zero padding to make the base and surface time histories the same length, as discussed below. The beginning of the surface noise window was calculated by subtracting the length of the surface signal window (t_{Sf} - t_{Si}) from the catalog event start time (refer to Figure 3a). This resulted in signal and noise windows for the surface DH_0 sensor of equivalent length.

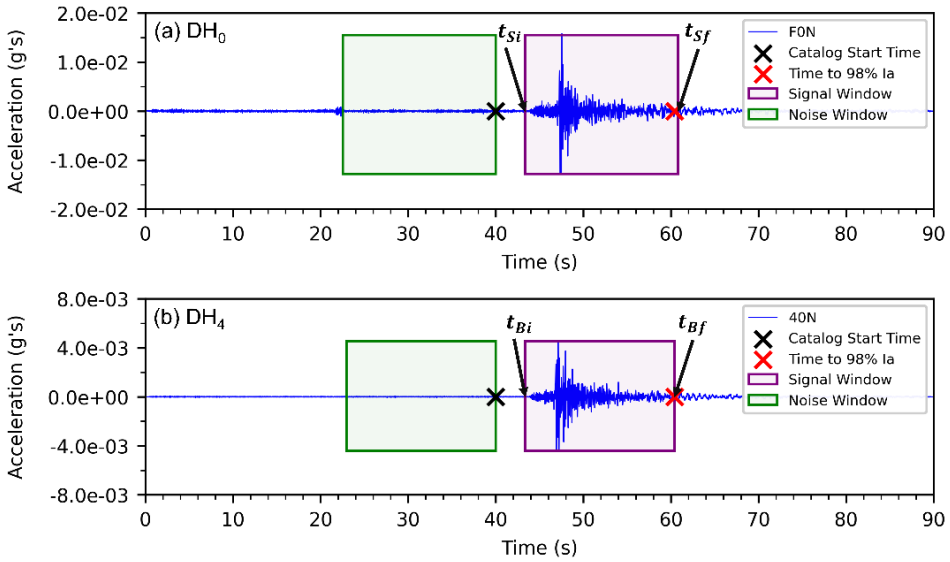


Figure 3. Illustration of the north component signal and noise windows of USGS Event ID uu60364822 recorded by the I15DA. Plot (a) shows the surface sensor DH_0 windows, and plot (b) shows the base sensor DH_4 (120 m) windows.

After dividing the time histories into signal and noise windows, the base and surface sensors were processed in the same manner. A Tukey cosine taper with a width of 5% of the time history was applied on both ends of the signal and noise windows. Then, the trailing end of the window was padded with zeros to the next-greater power of two to force the surface and deepest sensor windows to the same length, ensuring the same frequency resolution. Using a Fourier transformation, the Fourier amplitude spectrum (FAS) was calculated for each window. This FAS was resampled from frequencies of 0.1 to 100 Hz on a logarithmic scale with a total of 512 points. It was then smoothed using a Konno and Ohmachi smoothing window with a bandwidth of 40 (Konno and Ohmachi, 1998). An example of the processed signal and noise window FAS for the 120-m sensor is shown in Figure 4a.

After smoothing, the signal-to-noise (SNR) was calculated by dividing the signal FAS by the noise FAS (see Figure 4b). The usable bandwidth of the FAS for each base and surface station during each event was specified to be where the SNR was greater than 3.0. At this stage, ground motions from six additional aftershock events were discarded because they produced limited usable bandwidth on either the base or surface sensors due to a low SNR across the FAS. This left ground motions from a total of eight events for consideration in the ETF calculations. USGS event ID's, magnitudes, and PGA values for all of these ground motions are provided in Table 1.

One goal of this research was to establish a representative small-strain ETF for the I15DA that could be compared with linear-viscoelastic theoretical transfer functions (TTFs) obtained from ground response analyses. To ensure that the small-strain ETFs accurately represented only the

© ASCE

linear-viscoelastic behavior of the soil column, ground motions from the final eight candidate events were further screened based on the maximum shear strains they induced when propagated through a 1D soil model. Shear strain modeling was performed by propagating each horizontal component of all candidate ground motions from the DH_4 sensor through a soil model defined by the simplified PS-logging Vs profile and small-strain damping ratios obtained from Darendelli (2001). This 1D wave propagation modeling was performed using linear-viscoelastic time series analyses in the open-source site response software Strata (Kottke and Rathje, 2008). The two largest magnitude events (i.e., USGS Event IDs uu60369062 and uu60364832, with magnitudes of 4.57 and 3.94, respectively) produced simulated maximum shear strains that approached near-to, or exceeded, 0.01% in some of the soft, shallow soil layers, as depicted in Figure 5. These shear strains are approximately one order of magnitude higher than those typically associated with linear soil behaviour (Darendelli 2001) and indicate that these events likely induced some limited non-linear soil behaviour at the I15DA. As such, ground motions from these two events were rejected from consideration for calculating small-strain ETFs. Ground motions from the other six events induced maximum shear strains that were closer to 0.001% in the softest surficial soils. Thus, the final suite of small-strain ground motions consists of six events recorded on each horizontal component (North and East) with a usable bandwidth of 0.5 to 10 Hz. These events had magnitudes that ranged from 2.88 to 3.41 and PGA values that ranged from 0.002 to 0.012 g's, as indicated in Table 1. While the ground motions from the two largest events were not included in calculations for the representative linear-viscoelastic ETF, they are still important ground motions for larger strain ground response modelling. Thus, ground motions from all eight of the events that passed the SNR criteria over a bandwidth from 0.5 to 10 Hz are included in the processed ground motion database.

Table 1. Tabulated USGS event information for eight aftershock ground motions with distinguishable signal above background noise and usable frequency bandwidths between 0.5 and 10 Hz.

USGS Event ID	UTC Event Time	Mag.	Mag. Type	DH_4 PGA, *g's* (NS / EW)	DH_1 PGA, *g's* (NS / EW)
uu60364822	2020-03-18T19:07:30.25	3.41	M_L	0.00459 / 0.00360	0.01579 / 0.01197
uu60364832[1]	2020-03-18T19:12:23.61	4.57	M_W	0.02411 / 0.04296	0.07915 / 0.07446
uu60365152	2020-03-18T21:11:10.74	2.88	M_L	0.00327 / 0.00181	0.00866 / 0.00549
uu60366502	2020-03-19T12:44:47.70	3.2	M_L	0.00260 / 0.00605	0.01202 / 0.01187
uu60368447	2020-03-21T16:59:31.93	3.37	M_L	0.00364 / 0.00188	0.00903 / 0.00866
uu60369062[1]	2020-03-23T01:17:15.31	3.94	M_L	0.00701 / 0.00944	0.02438 / 0.03213
uu60370427	2020-03-26T16:12:42.89	3.25	M_L	0.00361 / 0.00291	0.00936 / 0.01040
uu60370437	2020-03-26T16:21:56.75	2.95	M_L	0.00116 / 0.00151	0.00359 / 0.00354

[1]Ground motions induced shear strains larger than 0.001% in some soil layers and were excluded from the small-strain ETF calculations.

CALCULATING THE EMPERICAL TRANSFER FUNCTION

After determining the small-strain ground motion suite, individual ETFs were calculated by dividing the FAS of the surface signal window for a given horizontal component by the corresponding FAS of the base signal window for the same horizontal component for each ground

© ASCE

motion event in the suite. The ETFs for each component of each small-strain event are shown in Figure 6. Since the individual ETFs from the North and East components of the I15DA sensors were found to be similar for any given event, the ETFs for each component were ultimately combined by calculating the geometric mean of both components (the square root of the product of the North and East components) in the frequency domain. The geometric mean ETFs for each individual event were then used to calculate a lognormal median ETF from all events, LM_{ETF}, and the associated standard deviation across events, $\sigma_{ln,ETF}$, as shown in Figure 6. The fundamental frequency of the ETF, $f_{0,ETF}$, and associated lognormal standard deviation, $\sigma_{f_{0,ETF}}$, was computed by taking the lognormal median of the frequencies associated with the highest peak from each individual North and East component ETF from 0.6 to 1.0 Hz. From the final suite of small-strain ground motions, the $f_{0,ETF}$ is 0.81 Hz with a $\sigma_{f_{0,ETF}}$ of 0.17.

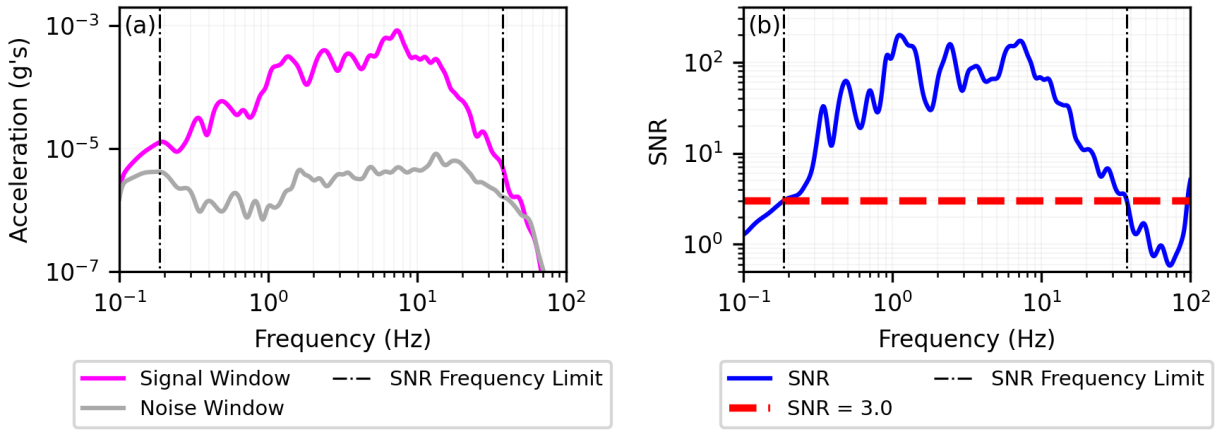


Figure 4. (a) North component signal and noise window FAS, and (b) SNR for processed USGS Event ID uu60364822 recorded by the DH4 120-m downhole sensor at the I15DA. The dotted red line on the SNR plot signifies a SNR of 3.0, and the dotted black lines on both plots denote the useable frequency bandwidth based on the SNR of 3.0.

The small-strain LM_{ETF} and individual aftershock ETFs are published alongside the raw and processed ground motions in an open-access database on DesignSafe. While the database is still in the process of being published at the time of writing this paper, one will be able to find it on DesignSafe by searching for "I-15 Downhole Array (I15DA)".

COMPARISON WITH 1D LINEAR-VISCOELASTIC SITE RESPONSE

The small-strain LM_{ETF} described in this paper is compared with the 1D linear-viscoelastic theoretical transfer function (TTF) obtained from the nine-layer simplified PS-logging Vs profile in Figure 6. This TTF calculation is detailed in Jackson (2024). The calculation for the TTF shown in Figure 6 was performed using a 1D linear-viscoelastic analytical solution coded in a Python script developed within the Cox research group at Utah State University, which has been validated against 1D linear-viscoelastic calculations in the program DEEPSOIL (Hashash et al., 2020). Small-strain damping, D_{min}, ranged from 2.0% near the surface to 0.7% near the base sensor using assumed soil properties for each layer and the relationships provided in Darendelli (2001). Because

© ASCE

the ETF represents the site response between 120 m and the surface, “within” conditions were specified for calculating the TTF.

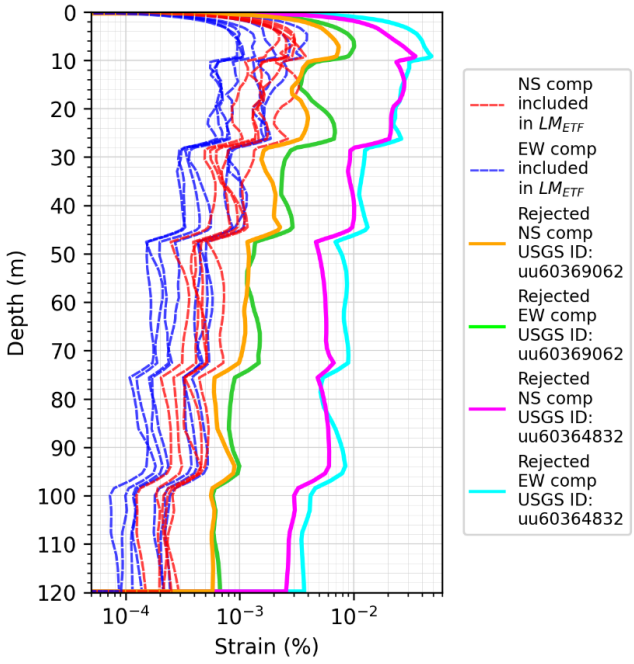


Figure 5. Shear-strain profiles generated using ground motions from the final eight candidate events with usable frequency bandwidths from 0.5 to 10 Hz. Ground motions that generated the largest shear strains (i.e., USGS event IDs uu60369062 and uu60364832) were not used for calculating the small-strain ETFs and the LM_{ETF}.

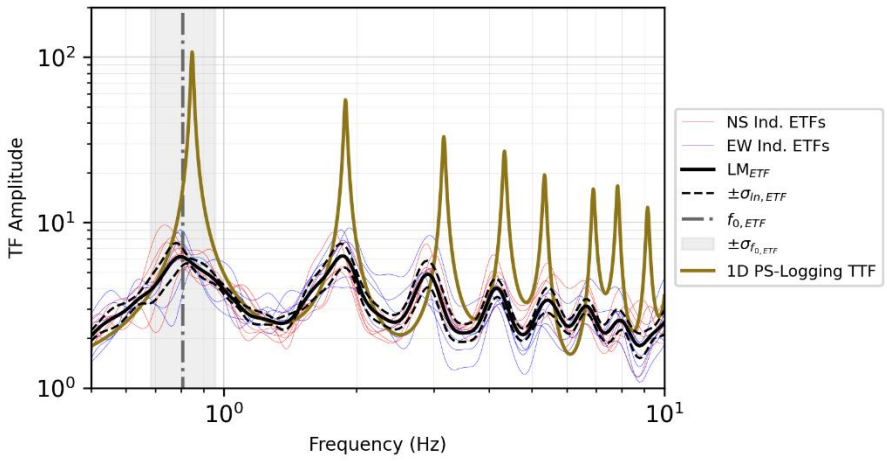


Figure 6. Empirical Transfer Functions (ETFs) from 120 m to the surface based on small-strain ground motions recorded by the I15DA. The LM_{ETF} is calculated by combining the individual North/South (red) and East/West (blue) ETFs into a geometric mean and then calculating the lognormal median of the combined ETFs. The fundamental frequency, $f_{0,ETF}$, and its associated lognormal standard deviation, $\sigma_{f_{0,ETF}}$, are shown in gray.

© ASCE

Visually, the TTF derived from the nine-layer simplified PS-logging Vs profile fits the resonant peaks in the LM_{ETF} quite well. The TTF captures the frequencies of the first two modes very well, but struggles to perfectly capture the higher mode frequencies. Additionally, the amplification ratios suggested by the TTF are significantly higher than those of the LM_{ETF} and overestimate by a factor of nearly 18 at the fundamental frequency. This characteristic of 1D linear-viscoelastic TTFs estimating the frequencies of the LM_{ETF} reasonably well but overpredicting the amplification ratios compared to the ETFs is well documented at other borehole array sites (e.g., Hallal et al., 2022). Jackson (2024) details further efforts to better predict site response at the I15DA using various 1D GRA approaches meant to account for spatial variability. We anticipate other researchers interested in site response at borehole arrays will benefit from the site characterization data, aftershock ground motion records, and ETFs documented herein.

CONCLUSIONS

This paper has described aftershock ground motions recorded by the I15DA following the M5.7 2020 Magna Earthquake. After processing the recordings, ground motions from eight aftershock events were determined to have SNR > 3 over a bandwidth from 0.5 to 10 Hz on both horizontal components of the surface (DH_0) and 120-m deep (DH_4) accelerometers. The two largest magnitude events (i.e., M_L 4.57 and 3.94) produced simulated maximum shear strains that approached near-to, or exceeded, 0.01% in some of the soft, shallow soil layers. These shear strains are approximately one order of magnitude higher than those typically associated with linear soil behaviour and indicate some limited non-linear soil behaviour was induced at the I15DA by these two events. As such, ground motions from these two events, while valuable for other purposes, were not considered for calculating small-strain ETFs. The final suite of ground motions used for calculating the small-strain ETFs originated from the remaining six aftershock events with magnitudes that ranged from 2.88 to 3.41 and PGA values that ranged from 0.002 to 0.012 g's. The ground motions and ETFs documented in this paper are a valuable resource for site response studies. As such, they are in the process of being added to an open-access database on DesignSafe, as described below.

DATA AVAILIBILITY

The ground motion and ETF data discussed in this paper is currently in the process of being added to a database on DesignSafe (Rathje et al. 2017) where it will be published alongside site characterization data including active and passive surface wave testing, deep (e.g. 1 km) 1D Vs profiles obtained through surface wave inversions, and single station ambient vibration time histories (for use with HVSR processing). We do not currently have a DOI associated with the database, but in the near future it will be able to be found by searching for "I-15 Downhole Array (I15DA)" on DesignSafe.

ACKNOWLEDGMENTS

We would like to thank Mr. Jon Rusho from the University of Utah Seismograph Stations (UUSS) for providing the aftershock ground motions from the I15DA, which we have processed and included in this open-source database.

© ASCE

REFERENCES

Darendeli, M. 2001. *Development of a new family of normalized modulus reduction and material damping curves*, [Ph.D.dissertation]. University of Texas at Austin.

Goulet, C. A., et al. 2021. "PEER NGA-East Database." *Earthquake Spectra*, 37(SI), 1331–1353.

Hallal, M. M., Cox, B. R., and Vantassel, J. P. 2022. "Comparison of State-of-the-Art Approaches Used to Account for Spatial Variability in 1D Ground Response Analyses". *Journal of Geotechnical and Geoenvironmental Engineering*, 148(5), Article 04022019.

Halling, M. W., and Petty, T. 2001. "Strong motion instrumentation of I-15 Bridge C-846." UDOT Report No. UT-01.12, Utah Dept. of Transportation, Salt Lake City, UT.

Hashash, Y. M. A., Musgrove, M. I., Harmon, J. A., Ilhan, O., Xing, G., Numanoglu, O., Groholski, D. R., Phillips, C. A., and Park, D. 2020. *DEEPSOIL 7.0, User Manual*. Urbana, IL, Board of Trustees of University of Illinois at Urbana-Champaign.

Jackson, T. S. 2024. "Evaluating 1D and 2D Small-Strain Ground Response Analyses at the I-15 Downhole Array Using Recorded Aftershocks from the M5.7 2020 Magna, Utah Earthquake". All Graduate Theses and Dissertations, Fall 2023 to Present, 197. https://digitalcommons.usu.edu/etd2023/197.

Kottke, A. R., and Rathje, E. M. 2008. "Technical manual for Strata." Report No. 2008/10, Pacific Earthquake Engineering Research Center, Univ. of California, Berkeley, CA.

Magistrale, H., Olsen, K. B., and Pechmann, J. C. 2008. "Construction and verification of a Wasatch front community velocity model". Technical report no. HQGR.060012, 14 pp, US Geological Survey, Reston, VA.

QGIS.org. 2025. QGIS Geographic Information System. QGIS Association. http://www/qgis.org.

Rathje, E. M., et al. 2017. "DesignSafe: New Cyberinfrastructure for Natural Hazards Engineering," *Natural Hazards Review*, 18, 06017001.

USGS. "Search Earthquake Catalog." https://earthquake.usgs.gov/earthquakes/search/. Accessed July 11, 2023.

UGRC (Utah Geospatial Resource Center). 2020. "Utah Quaternary Faults." Accessed April 20, 2025 at: https://opendata.gis.utah.gov/datasets/utahDNR::utah-quaternary-faults/about.

Youd, T. L., and Briggs, D. H. 2003. "Downhole seismic array at the intersection of I-15, I-80 and SR-201, Salt Lake City, Utah." UDOT Report No. UT-13.18, Utah Dept. of Transportation, Salt Lake City, UT.

© ASCE

A Dataset of Microtremor Horizontal-to-Vertical Spectral Ratio (mHVSR) Measurements Collected at Strong Motion Stations that Recorded the 2020 M5.7 Magna, Utah, Earthquake

Kyle S. Cannon[1] and Brady R. Cox, Ph.D.[2]

[1]Graduate Researcher, Dept. of Civil and Environmental Engineering, Utah State Univ.
Email: kyle.cannon@usu.edu
[2]Professor, Dept. of Civil and Environmental Engineering, Utah State Univ.
Email: brady.cox@usu.edu

ABSTRACT

Horizontal-to-vertical spectral ratio (HSVR) measurements of microtremors/ambient noise (i.e., mHVSR) are an inexpensive and effective way of estimating the resonant frequency (f_0) of sites that have strong subsurface impedance contrasts. Accurately estimating f_0 is an important step in modeling local ground motion site amplification during earthquakes, and numerous efforts are underway to incorporate mHVSR measurements into ground motion models (GMMs) as an additional constraint on site term parameters. As such, there is a need to provide mHVSR measurements at strong motion stations (SMS) that contribute important ground motion recordings to databases used for GMM development. One such set of important ground motion recordings was obtained during the 2020 M5.7 Magna, Utah, Earthquake, which occurred on the Wasatch Fault. We have made mHVSR measurements at 29 of the 32 SMS that recorded the Magna Earthquake with a peak ground acceleration (PGA) value of greater than 0.04 g. These SMS locations represent a wide variety of site conditions, from rock to deep, soft soils. The purpose of this paper is to present the mHVSR curves obtained from processing the ambient-noise data collected at each SMS site and to publicly share the data for broader use.

INTRODUCTION

Most current GMMs account for local site effects using one or more of the following three parameters: (1) Vs30, the time-averaged shear wave velocity over the top 30 meters; (2) Z1.0, the depth to a layer with a shear wave velocity (Vs) greater than 1 km/s; and (3) Z2.5, the depth to a layer with Vs greater than 2.5 km/s. Z1.0 and Z2.5, while valuable and informative for constraining site effects, can be challenging to work with in practice because obtaining reliable estimates of these parameters is not trivial, and the associated uncertainties can be quite large. As a result, most people often rely heavily on Vs30 to characterize site effects and use default values for Z1.0 and Z2.5. This isn't ideal because Vs30, which is useful to account for near-surface site properties, does not extend deep enough to capture site resonance effects at sites where the depth to a site-response-governing impedance contrast (e.g., bedrock below lakebed sediments) is greater than 30 m. For this reason, mHVSR measurements, which provide a rapid and cost-effective method for gathering information about the fundamental frequency of sites with strong subsurface impedance contrasts, are an attractive addition to GMM development and application.

Numerous efforts are currently underway to incorporate HVSR measurements —both earthquake-based HVSR (eHVSR) and mHVSR— into GMMs as an additional constraint on site term parameters (e.g., Pinilla-Ramos et al., 2022; Zaker et al., 2022; Yazdi et al., 2023; Zhang et al., 2025). To help with these efforts, it is essential to make mHVSR measurements at SMS that

© ASCE

contribute important ground motion recordings to databases used for GMM development. The ground motions recorded during the 2020 M5.7 Magna, Utah Earthquake event are of special interest, given that the Wasatch Fault is a normal fault, and normal faults are relatively under-represented in GMM databases.

The 2020 M5.7 Magna, Utah Earthquake mainshock occurred on March 18, 2020, shortly after 07:00 am local time. Over 2,500 aftershocks were observed after the mainshock, including two M4.6 events; one at 08:02 am and the other at 01:12 pm. The Magna Earthquake mainshock was recorded by 47 SMS within approximately 40 miles of the epicenter. A total of 32 stations recorded peak ground acceleration (PGA) values greater than 0.04 g. PGA values greater than 0.2 g were recorded at 11 stations, with a maximum PGA value of 0.43 g being recorded at the Lee Kay Center (LKC) station. We have made mHVSR measurements at 29 of the 32 SMS that recorded PGA values greater than 0.04 g (the remaining three stations —FTT, NOQ, and CTU— were inaccessible at the time of testing); the locations of these 29 stations are shown in Figure 1, where the points are color-coded by the PGA recorded during the 2020 M5.7 Magna, Utah Earthquake (PGA values obtained from Wong et al., 2021). The PGA values are tabulated in Table 1.

DATA ACQUISITION

Three-component broadband seismometers with a flat frequency response between 120 seconds and 100 Hz (Nanometrics Inc. Trillium Compact Horizon 120s) were used to record ambient vibrations. Seismometers were oriented to magnetic north and buried in shallow holes, backfilled with sand when native soil was unsuitable, and covered with a weighted bucket to improve coupling and reduce wind/temperature effects. Acquisition systems for the Trillium Compact 120s seismometers were Nanometrics Inc. Pegasus digitizers (24-bit ADC, 135 dB dynamic range, internal clock, and GPS receiver accurate to <100 μs).

At each of the 29 SMS sites, three hours of ambient noise was recorded at a sampling frequency of 100 Hz. Because broadband seismometers can take a little bit of time to settle directly following installation, the first hour was treated as “settling time”, and the last two hours were used as mHVSR data. The approximate distance from each sensor to the corresponding SMS is tabulated in Table 1. In all cases, the sensor was within 100 m of the SMS, and in all but two cases, the sensor was within 50 m.

DATA PROCESSING

At each broadband station location, mHVSR data were processed following the procedures documented in Cox et al. (2020), wherein a frequency-domain window-rejection algorithm is used to reject contaminated time windows, and a lognormal distribution is used to calculate statistics for fundamental site frequency obtained from the horizontal-to-vertical spectral ratio (i.e., $f_{0H/V}$).

The open-source Python package *hvsrpy* (Vantassel, 2020) was used for all mHVSR processing. First, a high-pass filter with a corner frequency of 0.005 Hz was applied in the time domain to each two-hour ambient noise recording on each of the three components (i.e., NS, EW, and Vert). Then, each time history for each component was divided into 90-second time windows (80 windows total). Each window was then linearly detrended and tapered to zero using a Tukey window with a 5% taper at each end. The detrended time windows for each component were then transformed to the frequency domain using a Fourier transformation, and the Fourier amplitude spectrum (FAS) for each of the two horizontal components were combined using the geometric mean method. To remove spurious spikes in the resulting FAS, Konno and Ohmachi (1998) smoothing was applied with a smoothing constant (b) of 40, as recommended by Cox et al. (2020).

© ASCE

Finally, the horizontal-to-vertical spectral ratios of the FAS were computed for each time window and the lognormal median mHVSR curve was calculated.

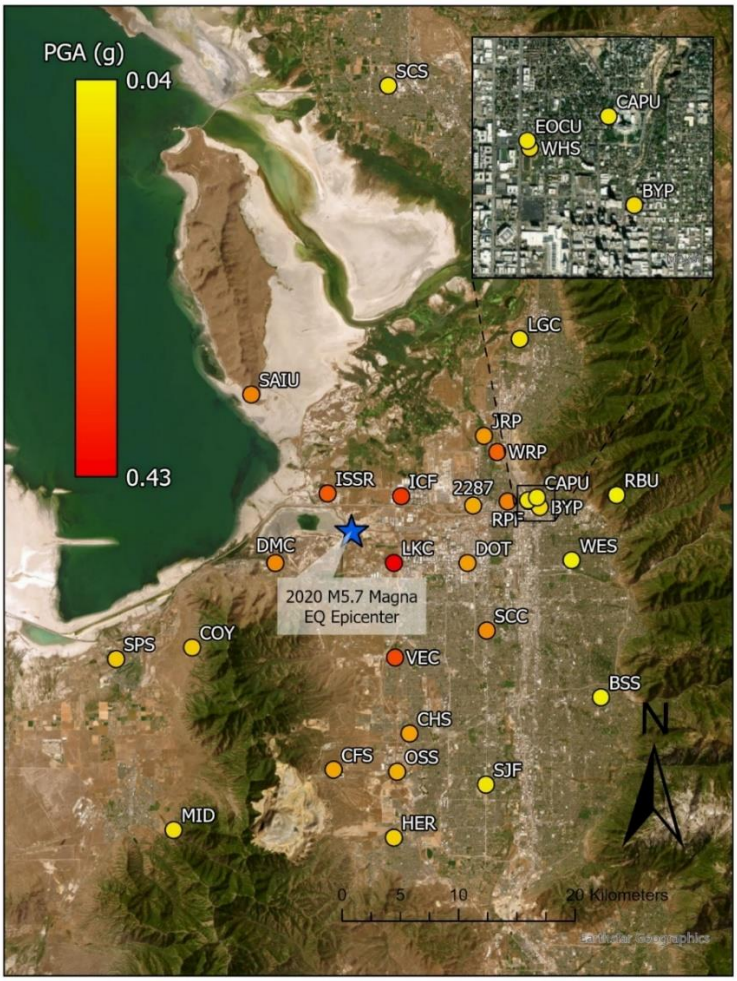


Figure 1: Map of the 29 SMS where mHVSR data were collected. The points are color-coded based on the PGA recorded during the 2020 M5.7 Magna, Utah Earthquake, as reported in Wong et al. (2021). PGA values range from 0.04 g to 0.43 g and are tabulated in Table 1. The epicenter of the Magna, Utah Earthquake is indicated with a blue star.

Historically, many researchers have chosen to obtain the mHVSR fundamental frequency from the lowest frequency peak of the lognormal median curve. In Cox et al. (2020), the frequency and amplitude associated with the lognormal median curves are referred to as $f_{0MC,H/V}$ and $A_{0MC,H/V}$, respectively. While informative, this lognormal median curve cannot be used to infer uncertainty/statistics about the actual f_0 values of each time window contributing to the median curve. For this reason, Cox et al. (2020) suggested calculating additional statistics on the actual f_0 values. These single-station $f_{0H/V}$ statistics are referred to as the lognormal median values (LM_{f0}) with associated standard deviation in natural log space ($\sigma_{ln,f0}$). Similarly, statistics can also be calculated on the amplitudes of the peaks, and these are referred to as LM_{A0} and $\sigma_{ln,A0}$. The range of frequencies that was searched for peaks during the mHVSR processing for each station are presented in Table 1.

© ASCE

RESULTS

Figure 2 shows the lognormal median mHVSR curve and the +/- one standard deviation curve for each station. The lowest frequency peak of each median curve is shown as a green diamond and the corresponding frequency and amplitude are referred to as $f_{0MC,H/V}$ and $A_{0MC,H/V}$, respectively. Also shown in each subplot are gray vertical lines representing the statistics for the distribution of the 80 individual f_0 values (i.e., LM_{f0} +/- $\sigma_{ln,f0}$).

The quality of each mHVSR peak was assessed by the SESAME reliability and clarity criteria (SESAME, 2004). There are three reliability criteria and six clarity criteria. If an mHVSR median curve peak does not pass all three reliability criteria, then the peak statistics should be used with caution. All median curve mHVSR peaks passed the three reliability criteria except for the one collected at the SAIU station; as such, the SAIU mHVSR statistics should be interpreted with caution. For this reason, the border of the SAIU plot is shown as dashed rather than solid. If, in addition to passing the three reliability criteria, a peak passes five or six of the clarity criteria, then the f_0 value can be considered as a very reliable estimate of the fundamental frequency (SESAME, 2004). Peaks that pass fewer than five criteria are considered less reliable. We used the SESAME clarity criteria, along with our own engineering judgment, to determine whether each peak was reasonable or unreasonable. The border color of each subplot in Figure 2 indicates the number of clarity criteria (out of 6) the peak passes; green corresponds to passing 5 or 6, orange to 4, red to 3, and gray to 2 or fewer. Peaks judged to be reasonable are shown with a green background, while unreasonable peaks are shown with a gray background. Peak statistics (i.e., LM_{f0}, $\sigma_{ln,f0}$, LM_{A0}, $\sigma_{ln,A0}$, $f_{0MC,H/V}$, and $A_{0MC,H/V}$) were calculated for all reasonable peaks and are reported in Table 1.

DISCUSSION

The most simple and useful way to present mHVSR data is a summary table of peak statistics ($LM_{f0,H/V}$ and $\sigma_{ln,f0}$) such as Table 1; however, it is also important to study the shapes of the mHVSR curves, and to analyze the individual horizontal and vertical FAS to better understand why the mHVSR curves are shaped the way they are. The SESAME clarity criteria provide a quantitative way to describe the shape/quality of the mHVSR peaks, but even peaks that pass the same number of SESAME clarity criteria can come from a wide range of curves. We will begin by discussing the $LM_{f0,H/V}$ values, and then we will discuss the mHVSR curve shapes and the individual horizontal and vertical FAS.

Figure 3 is a map of the 20 SMS with a reasonable mHVSR peak, color-coded by $LM_{f0,H/V}$. The other 9 SMS are shown for reference as small gray points. All else being equal, we would expect f_0 to decrease as the depth to bedrock increases. As such, we would expect higher $LM_{f0,H/V}$ values for stations closer to the mountains, and lower $LM_{f0,H/V}$ values for stations in the valley. We see this trend somewhat, except for with stations 2287 and DOT, where we have two valley stations with higher values of $LM_{f0,H/V}$ relative to the other stations. Interestingly, the range in $LM_{f0,H/V}$ values (0.27-0.76 Hz) is smaller than one might expect for a deep sedimentary basin. Of course, some of the stations have higher frequency peaks that we have not identified as fundamental (e.g., EOCU and WHS), and stations on rock do not have any peaks (e.g., COY and MID). Sgattoni and Castellaro (2020) explain that the sedimentary infill of deep and narrow valleys can tend to resonate as a whole at a single resonant frequency. While it is not certain that this is the case for the Salt Lake Valley, it is important to note.

© ASCE

Table 1: Summary Table of PGA Values and mHVSR Peak Statistics for Each of the 29 SMS Sites

Station ID	PGA[1] (g)	Approx. Distance from SMS[2] (m)	SESAME Criteria Passed	Search Range (Hz)	$LM_{f0,H/V}$ (Hz)	$\sigma_{ln,f0,H/V}$ (Hz)	$LM_{A0,H/V}$	$\sigma_{ln,A0,H/V}$	$f_{0MC,H/V}$ (Hz)	$A_{0MC,H/V}$
2287	0.153	50	4	0.3-10	0.564	0.176	4.357	0.179	0.607	3.226
BSS	0.043	30	4	0.3-10	0.408	0.146	7.591	0.615	0.435	5.663
BYP	0.081	5	4	--	--	--	--	--	--	--
CAPU	0.059	30	5	0.3-10	0.472	0.125	8.474	0.346	0.473	6.674
CFS	0.161	20	3	--	--	--	--	--	--	--
CHS	0.168	25	3	--	--	--	--	--	--	--
COY	0.105	5	1	--	--	--	--	--	--	--
DMC	0.206	10	5	0.3-10	0.495	0.134	2.909	0.234	0.460	2.274
DOT	0.170	35	4	0.3-10	0.567	0.125	4.269	0.192	0.590	3.254
EOCU	0.062	55	4	0.3-10	0.408	0.143	11.964	0.450	0.423	9.216
HER	0.094	25	4	--	--	--	--	--	--	--
ICF	0.338	25	6	0.3-10	0.473	0.071	8.134	0.203	0.460	7.006
ISSR	0.281	10	4	0.2-10	0.267	0.120	5.015	0.213	0.279	3.927
JRP	0.179	20	4	0.2-10	0.265	0.114	6.040	0.228	0.243	4.570
LGC	0.069	40	3	0.3-10	0.650	0.167	4.818	0.175	0.590	3.818
LKC	0.429	85	4	0.3-10	0.412	0.157	16.863	0.341	0.411	12.778
MID	0.072	5	2	--	--	--	--	--	--	--
OSS	0.143	15	3	--	--	--	--	--	--	--
RBU	0.044	10	4	0.3-5	0.533	0.158	4.796	0.361	0.590	3.632
RPF	0.217	35	3	0.3-10	0.739	0.154	4.221	0.160	0.758	3.397
SAIU	0.215	10	4	0.3-10	0.458	0.159	6.250	0.566	0.514	4.803
SCC	0.201	10	4	0.5-10	0.757	0.196	3.988	0.132	0.895	3.116
SCS	0.067	45	4	0.3-10	0.435	0.187	5.402	0.379	0.411	4.178
SJF	0.060	20	3	--	--	--	--	--	--	--
SPS	0.109	5	5	0.3-10	0.499	0.105	5.073	0.226	0.500	4.234
VEC	0.308	25	5	0.3-10	0.410	0.143	6.296	0.404	0.447	4.796
WES	0.048	30	4	--	--	--	--	--	--	--
WHS	0.087	45	5	0.3-10	0.380	0.113	8.683	0.379	0.379	6.807
WRP	0.269	20	5	0.3-10	0.345	0.058	7.252	0.288	0.339	6.130

[1]PGA recorded during the 2020 M5.7 Magna, Utah Earthquake

[2]In some cases, the exact location of the SMS is unknown either because it is no longer in service or because of access restrictions; thus, some of these distances are very approximate

© ASCE

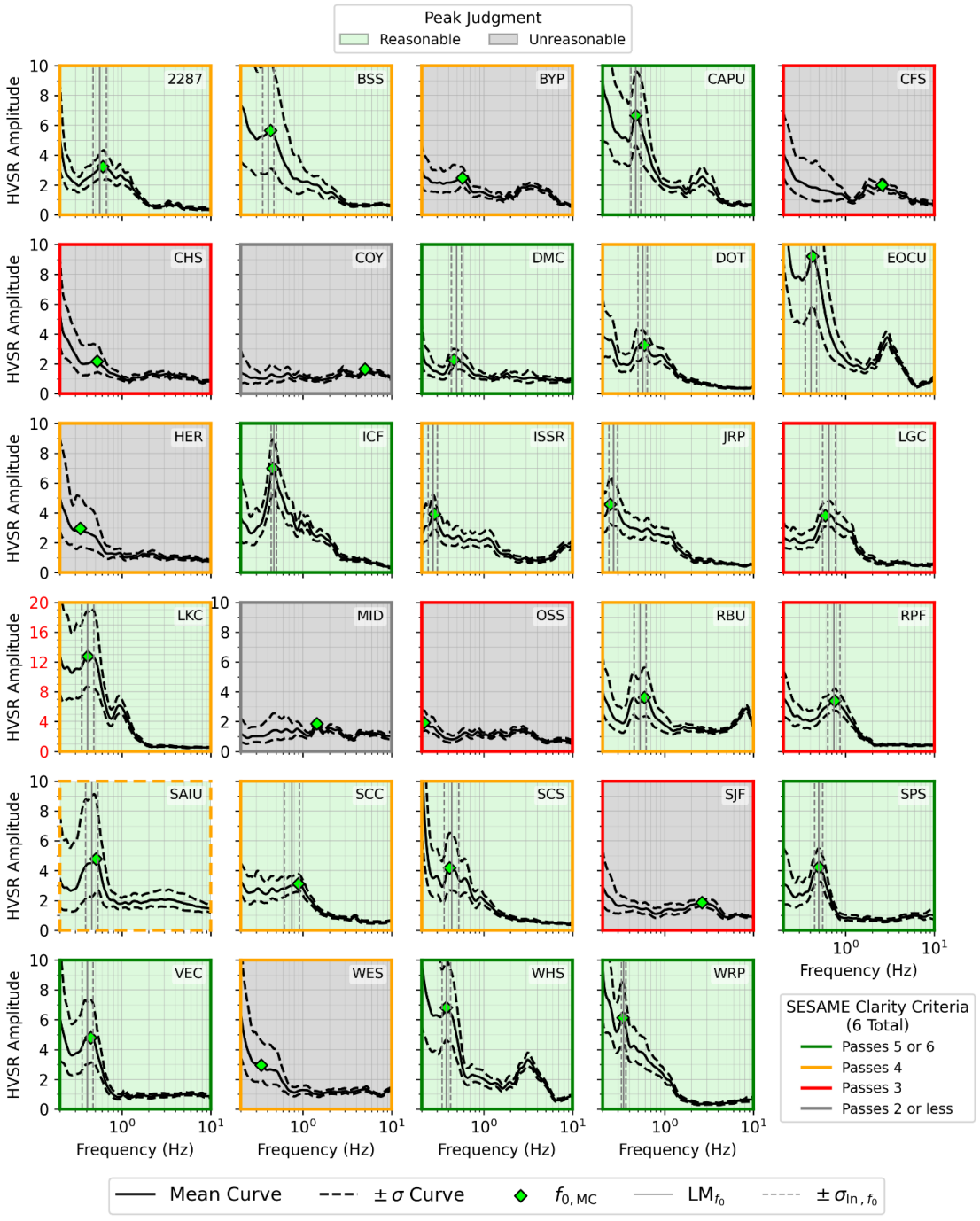


Figure 2: Lognormal median mHVSR curve and the +/- one standard deviation curve for each of the 29 SMS sites. The peak of each median curve is shown as a green diamond. Vertical gray lines represent the statistics for f_0 (LM_{f0} +/- $\sigma_{ln,f0}$) of all reasonable peaks. Reasonable peaks are shown with a green background and unreasonable peaks with a gray background. The border color of each subplot indicates the number of clarity criteria (out of 6) the respective peak passes; green corresponds to passing 5 or 6, orange to 4, red to 3, and gray to 2 or fewer. Note that the y-scale for the LKC subplot is different from the rest (0 to 20 instead of 0 to 10).

© ASCE

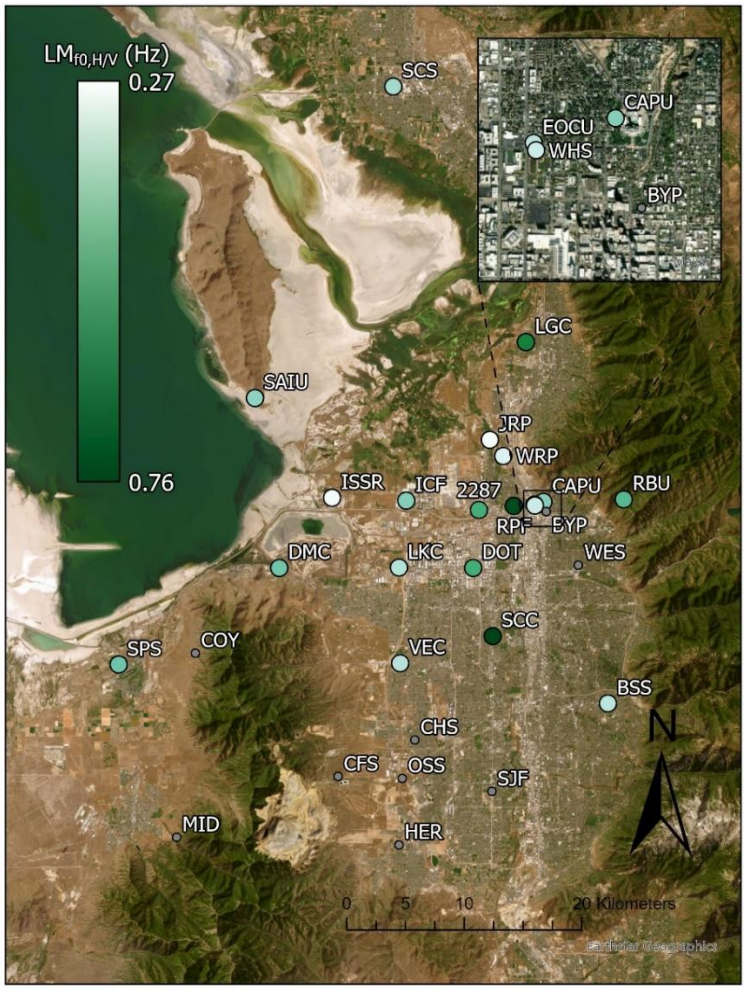


Figure 3: Map of the 29 SMS where mHVSR data were collected. For the 20 SMS peaks that were reasonable, stations are color-coded based on $LM_{f0,H/V}$. $LM_{f0,H/V}$ values range from 0.27 Hz to 0.76 Hz and are tabulated in Table 1. Each of the other 9 SMS is shown as a small gray point.

The mHVSR curves in Figure 2 vary widely in shape and complexity. Flat curves, such as the curves at stations COY, MID, OSS, and SJF, are often indicative of either shallow bedrock or the absence of a strong impedance contrast with depth (SESAME, 2004). Curves with a single narrow peak, such as the curves at stations ICF and SPS, represent a single large impedance contrast in the subsurface. Curves with two relatively narrow peaks, such as the curves at stations CAPU, EOCU, LKC, and WHS, suggest that there are two significant impedance contrasts with depth (SESAME, 2004). Curves with a broad single peak (e.g., LGC, RPF), a broad double peak (e.g., RBU, SCS), a broad band of amplification (e.g., BYP, SCC), or other characteristic shapes that can't be categorized as easily are more difficult to interpret. Their quality is more subjective. For example, at LGC and RPF, the peaks look reasonable, but because of uncertainty in the peak frequency, as evidenced by the broadness of the median curve, they only pass 3 of 6 clarity criteria. Many of the mHVSR curves show significant upward drift at frequencies below 0.3 or 0.2 Hz, which can make peaks near that range disappear or seem insignificant. This is something that we have noticed in mHVSR data for several years, and it is likely due to installation effects, wind

© ASCE

noise, temperature fluctuations (Doody et al., 2018) and pressure fluctuations (Bormann and Wielandt, 2013). We have found that burying the sensors 2-3 feet in the ground can help mitigate these effects, but it is not practical for temporary deployments.

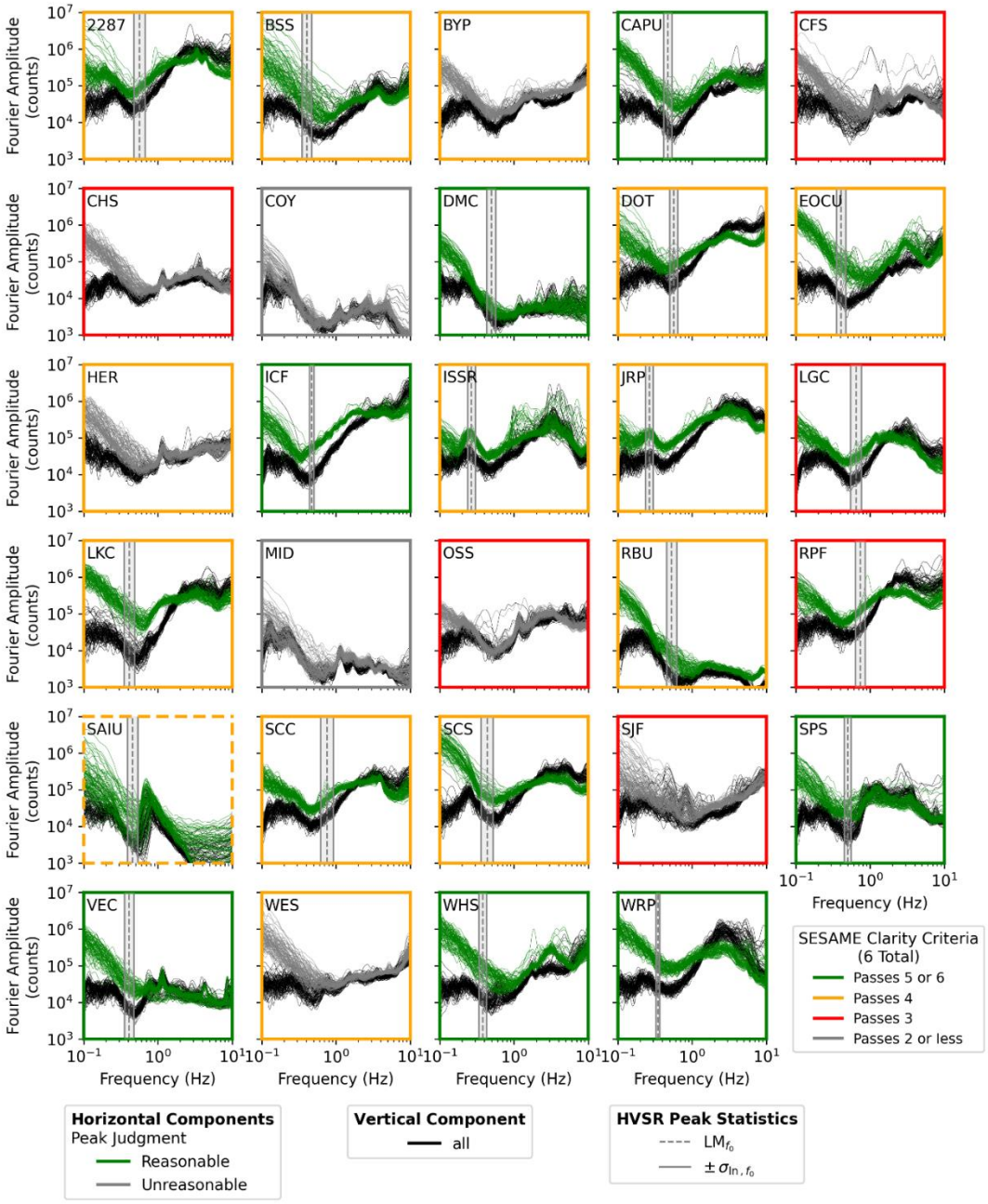


Figure 4: All 80 horizontal and vertical FAS for each of the 29 SMS sites. Vertical gray lines represent the statistics for f_0 (LM_{f0} +/- $\sigma_{ln,f0}$) of all reasonable peaks. Horizontal-component FAS curves are either green (stations with a reasonable peak) or gray (stations with unreasonable peaks). Vertical-component FAS curves are all black. The border color of each subplot indicates the number of clarity criteria (out of 6) the respective peak passes; green corresponds to passing 5 or 6, orange to 4, red to 3, and gray to 2 or fewer.

© ASCE

Figure 4 shows the individual horizontal and vertical FAS at each station. The combined horizontal component curves for each station are either green (stations with a reasonable peak) or gray (stations with unreasonable peaks), while the vertical component curves are all black. A few notable trends/patterns are observed: (1) the upward trend in mHVSR amplitude below frequencies of 0.2-0.3 Hz seems to be a product of an upward linear drift (in log-log space) in the horizontal components (e.g., HER and LKC); (2) some mHVSR peaks are a result of a dip in the vertical component (e.g., VEC and ICF), while other peaks are a result of a spike in the horizontal component (e.g., ISSR and JRP); (3) the best mHVSR peaks have horizontal and vertical FAS that form an "eye" of white, with clear separation of the horizontal and vertical components near the resonant peak that come back together at higher and lower frequencies (e.g., ICF). Research in this area is still ongoing.

CONCLUSIONS

This paper presents mHVSR data that was collected at 29 of the 32 SMS that recorded the 2020 M5.7 Magna, Utah Earthquake with a PGA of over 0.04 g. The data was processed using the open-source Python package *hvsrpy* (Vantassel 2020) and following the statistical processing methods documented in Cox et al. (2020). The quality of the mHVSR curves were assessed using the SESAME peak clarity and reliability criteria (SESAME, 2004), and engineering judgment. The raw and processed mHVSR data will soon be made publicly available on DesignSafe (Rathje et al., 2017), as described in the Data Availability Section, below. This dataset will be of value to those seeking to incorporate mHVSR measurements into GMMs as an additional constraint on site term parameters and is particularly valuable in contributing data to normal faulting environments.

DATA AVAILABILITY

The raw and processed mHVSR data documented in this paper are currently in the process of being added to a dataset on DesignSafe (Rathje et al., 2017), where it will be published open-access. While we do not currently have a DOI for this dataset, in the near future it will be able to be found by searching DesignSafe (https://www.designsafe-ci.org/) under the name, "A Dataset of Microtremor Horizontal-to-Vertical Spectral Ratio (mHVSR) Measurements Collected at Strong Motion Stations that Recorded the 2020 M5.7 Magna, Utah Earthquake".

ACKNOWLEDGMENTS

The mHVSR data documented in this paper were collected with funding from Pacific Gas and Electric (PG&E). While we gratefully acknowledge their support, any opinions, findings, or recommendations expressed in this article are those of the authors and do not necessarily reflect the views of PG&E.

REFERENCES

Bormann, P., and E. Wielandt. 2013. "Seismic signals and noise." In *New manual of seismological observatory practice 2 (NMSOP2)*, 1-62, Deutsches GeoForschungsZentrum GFZ.

© ASCE

Cox, B. R., T. Cheng, J. P. Vantassel, and L. Manuel. 2020. "A statistical representation and frequency-domain window-rejection algorithm for single-station HVSR measurements." *Geophys. J. Int.*, 221, 2170-2183.

Doody, C. D., A. Ringler, R. Anthony, D. Wilson, A. Holland, C. Hutt, and L. Sandoval. 2018. "Effects of thermal variability on broadband seismometers: Controlled experiments, observations, and implications." *Bull. of the Seismol. Soc. of Am.*, 108 (1), 493-502.

Konno, K., and T. Ohmachi. 1998. "Ground-motion characteristics estimated from spectral ratio between horizontal and vertical components of microtremor." *Bull. Seismol. Soc. Am.*, 88 (1), 228-241.

Pinilla-Ramos, C., N. Abrahamson, and R. Kayen. 2022. "Estimation of site terms in ground-motion models for California using horizontal-to-vertical spectral ratios from microtremor." *Bull. Seismol. Soc. Am.*, 112 (6), 3016-3036.

Rathje, E. M., et al. 2017. "DesignSafe: New Cyberinfrastructure for Natural Hazards Engineering," *Natural Hazards Review*, 18, 06017001.

SESAME. 2004. Guidelines for the Implementation of the H/V Spectral Ratio Technique on Ambient Vibrations Measurements, Processing, and Interpretation. European Commission – Research General Directorate, 62.

Sgattoni, G., and S. Castellaro. 2020. "Detecting 1-D and 2-D ground resonances with a single-station approach." *Geophys. J. Int.*, 223, 471-487.

Vantassel, J. P. 2020. *jpvantassel/hvsrpy : Latest (Concept)*. Zenodo. http://doi.org/10.5281/zenodo.3666956.

Wong, I., Q. Wu, and J. C. Pechmann. 2021. "The 18 March 2020 M 5.7 Magna, Utah, Earthquake: strong-motion data and implications for seismic hazard in the Salt Lake Valley." *Seismol. Res. Lett.*, 92 (2A), 773-786.

Yazdi, M., J. G. Anderson, and R. Motamed. 2023. "Reducing the uncertainties in the NGA-West2 ground motion models by incorporating the frequency and amplitude of the fundamental peak of the horizontal-to-vertical spectral ratio of surface ground motions." *Earthq. Spectra*, 39 (2), 1088-1108.

Zaker Esteghamati, M., A. R. Kottke, and A. Rodriguez-Marek. 2022. "A data-driven approach to evaluate site amplification of ground-motion models using vector proxies derived from horizontal-to-vertical spectral ratios." *Bull. Seismol. Soc. Am.*, 112 (6), 3001-3015.

Zhang, B., X. Lu, M. Rong, X. Kong, J. Wang, Y. Yu, and X. Li. 2025. "HVSR fpeak-based Vs30 estimation model and its applicability to GMPE in Southwest China." *Seismol. Res. Lett.*, XX, 1-10.

© ASCE